RSC Advances

RSC Publishing

PAPER

View Article Online
View Journal | View Issue

Cite this: *RSC Advances*, 2013, **3**, 5491

Enhanced near-infrared quantum cutting luminescence in 1,2,4,5-benzenetetracarboxylic acid/$NaYF_4$:Tb^{3+}, Yb^{3+} hybrid nanoparticles

Suwen Li,[ab] Zhiyao Hou,[a] Ziyong Cheng,[a] Hongzhou Lian,[a] Ping'an Ma,[a] Chunxia Li[a] and Jun Lin*[a]

Received 21st December 2012,
Accepted 31st January 2013

DOI: 10.1039/c3ra23439h

www.rsc.org/advances

The ultra-small-sized $NaYF_4$:Tb^{3+}, Yb^{3+} nanoparticles and hybrid L-$NaYF_4$:Tb^{3+}, Yb^{3+} (L: dehydro-1,2,4,5-benzenetetracarboxylic acid) nanoparticles have been prepared by a hydrothermal synthesis and water bath reflux method. X-Ray diffraction (XRD), transmission electron microscopy (TEM), high-resolution TEM (HRTEM), Fourier transform infrared (FTIR) spectra, UV-vis absorption spectra, diffuse reflectance spectra, photoluminescence (PL) spectra, as well as kinetic decay are used to characterize the resulting samples. The hybrid nanoparticles display a broad absorption band from 230 nm to 530 nm by monitoring $^2F_{5/2} \rightarrow {}^2F_{7/2}$ transition of Yb^{3+} at 977 nm. Upon the excitation of π–π^* transition of the organic 1,2,4,5-benzenetetracarboxylic acid (label with H_4L), the strong NIR emission at about 1000 nm that matches to energy of Si band gap of Si-based solar cells is obtained. As a downconversion luminescent converter, this kind of material might be useful in Si-based solar cells to reduce thermalization loss and enhance conversion efficiency of solar cells *via* spectral modification.

Introduction

Since the quantum cutting in Eu^{3+}–Gd^{3+} material was reported by Wegh *et al.*,[1] this kind of material has been widely investigated for applications in the noble gas discharge tube lamp source for the vacuum-UV to visible quantum cutting[1–4] and the solar cells for the visible to near infrared quantum cutting.[5–31] The latter has rapidly developed in recent years. By cutting one high energy photon into two or more low energy photons with energy close to the band gap of the Si solar cell (*i.e.* NIR QC), the thermalization losses can be reduced and the efficiency of solar cells can also be enhanced *via* modifying solar spectrum.

NIR QC can be realized by using coupled rare earth (RE) ions due to their unique energy level structures and high quantum efficiency. Presently, there are numerous reports in a variety of RE ions couples, including Tb^{3+}–Yb^{3+}, Tm^{3+}–Yb^{3+}, Pr^{3+}–Yb^{3+}, Nd^{3+}–Yb^{3+}, Er^{3+}–Yb^{3+}, Ce^{3+}–Yb^{3+} and Ho^{3+}–Yb^{3+} *etc.* Among them, the Tb^{3+}–Yb^{3+} ion couple became focus of research for NIR QC because the energy difference between the Tb^{3+} $^5D_4$ to $^7F_6$ energy levels is about twice that of the Yb^{3+} $^2F_{5/2}$ to $^2F_{7/2}$ transition, and the Yb^{3+} $^2F_{5/2}$ to $^2F_{7/2}$ emission (about 1000 nm) matches well with the band gap energy of Si. Moreover, the cooperative down-conversion by transfer from Tb^{3+} to Yb^{3+} ions has been tested to enhance the response of the photovoltaic solar cells.[12,13] For the matrices of NIR QC materials, there are a number of studies in fluorides, borates, phosphates and tungstate systems. Among them, fluorides are optimal host matrix materials for NIR QC due to their unique properties, such as low phonon energy, low refractive index, high ionicity, wide band gap, adequate thermal and environmental stability as well as large solubility for RE^{3+} ions. However, these RE^{3+} ion couples co-doped with fluorides for NIR QC also possess intrinsic limits, *i.e.*, there is no allowed absorbance in the UV region, thus limiting their practical application. Specially, f → f transitions of RE^{3+} ions doped in fluorides are Laporte forbidden. The principal disadvantage of RE^{3+} ions as phosphors is the low molar absorptivity (ε = 1–10 M^{-1} cm^{-1})[32] associated with 4f → 4f transitions and low absorption cross section (absorption cross section of Tb^{3+} in the order of 10^{-21} cm^2,[33] and no absorption for Yb^{3+} ions in UV-vis range), leading to inefficient optical excitation and low luminescence intensity.

Rare Earth (RE) organic/inorganic hybrid materials can take advantage of the beneficial properties of both materials of organic ligands and inorganic host materials. Briefly, the excitation wavelength used is in resonance with a strong ligands absorbance. The excited ligands then efficiently transfers its energy to the RE^{3+} ions and achieve efficient emission. This is so-called ''antenna effect'', which will allow for a large increase of the luminescence intensity through

[a]*State Key Laboratory of Rare Earth Resource Utilization, Changchun Institute of Applied Chemistry, Chinese Academy of Sciences, Changchun, 130022, P. R. China. E-mail: jlin@ciac.jl.cn; Tel: +86 0431 85262614*
[b]*College of Science, Changchun Institute of Technology, Changchun, 130012, P. R. China. E-mail: lswen@ ciac.jl.cn*

indirect excitation, and for the possibility to tune the absorption cross section into regions where the fluoride nanoparticles do not have absorption normally. The net result of so-called ''antennae effect'' is to increase the effective molar extinction coefficient of the phosphor complexes by several orders of magnitude.[34] At the same time, the inorganic fluorides matrixes protect RE^{3+} cations from sources of nonradiative deactivation, and the luminescence is enhanced.

Herein, in the paper, we prepared the hybrid materials of organic 1,2,4,5-benzenetetracarboxylic acid (H_4L) with inorganic $NaYF_4$:Tb^{3+}, Yb^{3+} nanoparticles for the first time. The structure, morphology, photoluminescence (PL) properties in UV-vis and NIR region, fluorescence decay dynamics of the hybrid materials are investigated systematically.

Experimental section

Chemicals and materials

The rare earth oxides RE_2O_3 (99.999%) (RE = Y, Tb, Yb) were purchased from Science and Technology Parent Company of Changchun Institute of Applied Chemistry, and other chemicals were purchased from Beijing Chemical Company. All chemicals are of analytical grade reagents and used directly without further purification. Rare earth nitrate stock solutions of 0.2 M were prepared by dissolving the corresponding rare earth oxides in dilute HNO_3 under heating with agitation.

Preparation of $NaYF_4$: 1 mol%Tb^{3+}, x mol%Yb^{3+} (x = 1, 3, 5, 10) nanoparticles

In a typical procedure for the preparation of $NaYF_4$: 1 mol%Tb^{3+}, 5 mol% Yb^{3+} nanoparticles, 13.16 mL $Y(NO_3)_3$ (0.2 M), 0.14 mL $Tb(NO_3)_3$ and 0.70 mL $Yb(NO_3)_3$ were added into 40 mL of aqueous solution containing 28 mmol of trisodium citrate (labeled as Cit^{3-}) to form a transparent solution under vigorous stirring. After vigorous stirring for 20 min, 20 mL of aqueous solution containing 8.4 mmol of NaF was introduced into the above solution. Then the mixing solution was transferred into a 100 mL Teflon autoclave, sealed, maintained 24 h at 180 °C and then allowed to cool to room temperature naturally. The resulting nanoparticles were precipitated by adding ethanol and separated from the suspension by centrifugation. The precipitates were washed thoroughly with ethanol and dried in vacuum at 75 °C overnight. The $NaYF_4$: 1 mol%Tb^{3+}, x mol%Yb^{3+} (x = 1, 3, 10) nanoparticles were prepared in a similar way as described above for the $NaYF_4$: 1 mol%Tb^{3+}, 5 mol%Yb^{3+} nanoparticles.

Preparation of H_4L/$NaYF_4$: 1 mol%Tb^{3+}, x mol%Yb^{3+} (x = 1, 3, 5, 10) hybrid nanoparticles

In a typical experiment, the appropriate amounts of 1,2,4,5-benzenetetracarboxylic anhydride were added into 40 mL of deionized water, and then 1 mL of ethanol was added to form transparent H_4L aqueous solution. The as-prepared $NaYF_4$: 1 mol%Tb^{3+}, x mol%Yb^{3+} nanoparticles were uniformly dispersed into H_4L aqueous solution. The solution was maintained at 65 °C for 4 h in a reflux system and then allowed to cool to room temperature. The resulting products were separated by centrifugation and washed three times with deionized water and dried in vacuum at 75 °C overnight.

Characterizations

X-Ray power diffraction (XRD) measurements were performed on a Rigaku-Dmax 2500 diffractometer at a scanning rate of 5 deg min^{-1} in the 2θ range from 15° to 80°, with graphite monochromatized Cu-Kα radiation (λ = 0.15405 nm). A transmission electron microscope (TEM, JEOL-2010, 200 kV) and high-resolution TEM (HRTEM) (FEI Tecnai G2 S–Twin transmission electron microscope) with a field emission gun operated at 200 kV were used. Fourier transform infrared (FTIR) spectra were recorded on a Perkin-Elmer 580B IR spectrophotometer in KBr pellets. The UV-vis absorption spectra were measured on a U-3310 scanning spectrophotometer. The diffuse reflectance spectra were measured with a UV-vis-NIR spectrophotometer (HITACHI U–4100). The UV-vis photoluminescence spectra were obtained by a Hitachi F-7000 spectrophotometer equipped with a 150 W xenon lamp as the excitation source. The NIR photoluminescence spectra were studied using an FLS-920 spectrometer. The decay curves measurements were performed by using a tunable laser (Continuum Sunlite OPO (pulse width = 4 ns)) as excitation source. The decay curves were obtained *via* a Lecroy Wave Runner 6100 digital oscilloscope (1 GHz). All measurements were performed at room temperature.

Results and discussion

Structure and morphology

The composition and phase purity of the nanoparticles were examined by XRD. Fig. 1 shows the representative XRD patterns of $NaYF_4$: 1 mol%Tb^{3+}, 5 mol%Yb^{3+}, L-$NaYF_4$: 1 mol%Tb^{3+}, 5 mol%Yb^{3+} and the standard JCPDS card (No. 06–0342), respectively. All diffraction peaks of the samples can be readily indexed to pure $NaYF_4$. Due to the small-size nature of the particles, a significant broadening of the diffraction peak is observed. Such relatively small sizes are compatible to use in

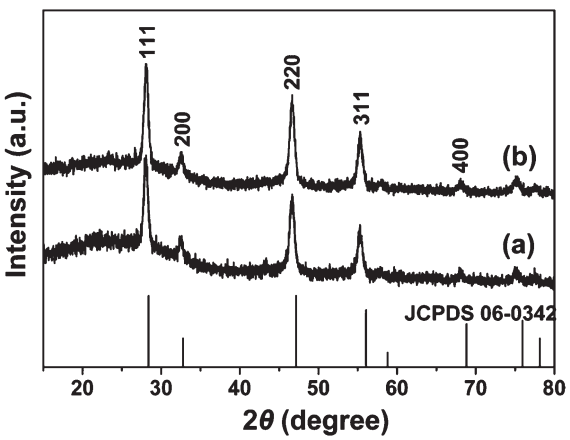

Fig. 1 XRD patterns of the $NaYF_4$: 1 mol%Tb^{3+}, 5%Yb^{3+} (a), L-$NaYF_4$: 1 mol%Tb^{3+}, 5%Yb^{3+} (b) and the standard JCPDS card 06-0342 of $NaYF_4$.

Table 1 The nanoparticle sizes estimated from the XRD data, fluorescence decay constant and lifetime of $^5D_4 \rightarrow {}^7F_5$ transition at 545 nm of Tb^{3+} ions

Samples	Diameter (nm)	Lifetime (ms)		Ratio constant	
		τ_1	τ_2	I_1	I_2
$NaYF_4$: 1%Tb^{3+}, 1%Yb^{3+}	2.71	0.697	1.525	0. 35	0.65
$NaYF_4$: 1%Tb^{3+}, 3%Yb^{3+}	2.70	0.619	1.388	0.38	0.62
$NaYF_4$: 1%Tb^{3+}, 5%Yb^{3+}	2.69	0.507	1.247	0.40	0.60
$NaYF_4$: 1%Tb^{3+}, 10%Yb^{3+}	2.66	0.381	1.191	0.44	0.56
L-$NaYF_4$: 1%Tb^{3+}, 1%Yb^{3+}	2.75	3.365	1.551	0.29	0.71
L-$NaYF_4$: 1%Tb^{3+}, 3%Yb^{3+}	2.74	3.355	1.454	0.31	0.69
L-$NaYF_4$: 1%Tb^{3+}, 5%Yb^{3+}	2.71	3.192	1.370	0.32	0.68
L-$NaYF_4$: 1%Tb^{3+}, 10%Yb^{3+}	2.70	2.777	1.275	0.32	0.68

light-converter of Si-based solar cells because small size can avoid optical scatter and improve light transmission of converter. The average size of nanoparticles was estimated for each as-prepared samples from the Scherrer formula, D = Kλ/βcosθ, where D is the average particle size, λ is the X-ray wavelength (0.15405 nm), β is the full-width at half-maximum, θ is the diffraction angle of an observed peak, K is a constant (0.89), respectively. The estimated average size of nanoparticles is listed in Table 1. In addition, all the diffraction peaks of RE^{3+} doped $NaYF_4$ samples have a slight shift to lower angle compared with the pure $NaYF_4$. This is because Tb^{3+} ion has a bigger radius than Y^{3+} ion (0.1095 nm for Tb^{3+} *vs.* 0.1075 nm for Y^{3+}).[35]

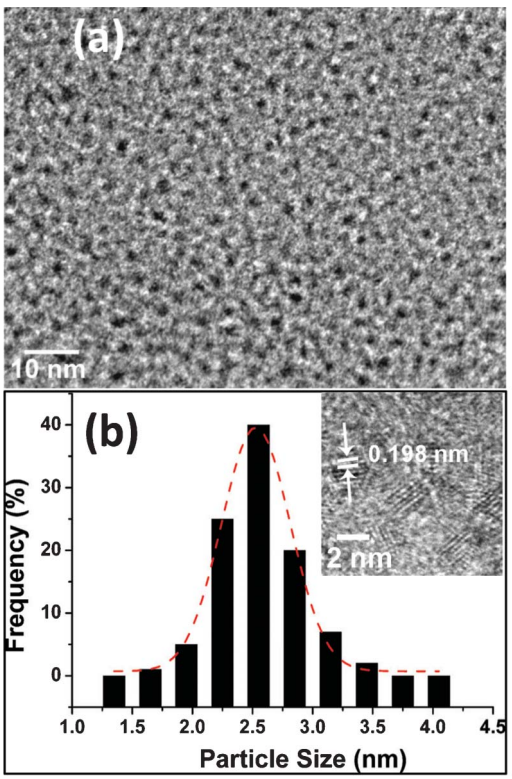

Fig. 2 TEM images (a) and histogram of diameter distribution (b) of $NaYF_4$: 1 mol%Tb^{3+}, 5%Yb^{3+} nanoparticles. (b) Inset: HRTEM images of $NaYF_4$: 1 mol%Tb^{3+}, 5%Yb^{3+} nanoparticles.

Fig. 2(a) shows the representative TEM image of $NaYF_4$: 1 mol%Tb^{3+}, 5 mol%Yb^{3+} sample. The results for other doping concentrations of Yb^{3+} in the $NaYF_4$: 1 mol%Tb^{3+}, *x* mol%Yb^{3+} (*x* = 1, 3, 10) and L-$NaYF_4$: 1 mol%Tb^{3+}, *x* mol%Yb^{3+} (*x* = 1, 3, 5, 10) samples are similar to result of $NaYF_4$: 1 mol%Tb^{3+}, 5 mol%Yb^{3+} and will not be shown here. From Fig. 2(a), it can be seen that the obtained nanoparticles are roughly spherical and monodisperse. Fig. 2(b) shows the statistics of diameter distribution of the $NaYF_4$: 1 mol%Tb^{3+}, 5 mol%Yb^{3+} nanoparticles. The nanoparticles size distribution is narrow. And the mean diameter of the nanoparticles is 2.6 nm (the total particles reach to 100), which is approximately consistent with the result of XRD. In the illustration of Fig. 2(b), the HRTEM image of nanoparticles clearly reveals the well-resolved diffraction fringes of the lattices, indicating that nanoparticles are highly crystalline. The lattice fringes with 0.198 nm spacing are clearly visible and in accordance with the lattice spacing of (2 2 0) of $NaYF_4$ crystal.

FTIR, UV-vis absorption and diffuse reflection

To demonstrate that the H_4L molecules had been bonded onto the nanoparticles, the FTIR, UV-vis absorption and diffuse reflection spectra were measured.

The representative FTIR spectra of the $NaYF_4$: 1 mol%Tb^{3+}, 5 mol%Yb^{3+} and L-$NaYF_4$: 1 mol%Tb^{3+}, 5 mol%Yb^{3+} are shown in Fig. 3. As shown in Fig. 3(a) , the broad band at 3447 cm^{-1} characterizing mode is appreciable for the O–H (COO–H)

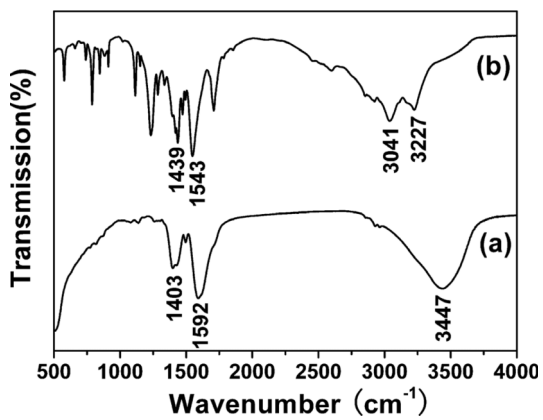

Fig. 3 FTIR spectra of $NaYF_4$: 1 mol%Tb^{3+}, 5%Yb^{3+} (a) and L-$NaYF_4$: 1 mol%Tb^{3+}, 5%Yb^{3+} (b).

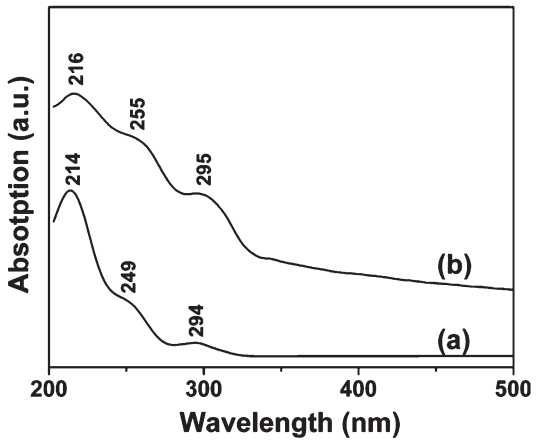

Fig. 4 UV-Vis absorption spectra of H_4L (a) and L-$NaYF_4$: 1 mol%Tb^{3+}, 5%Yb^{3+} (b).

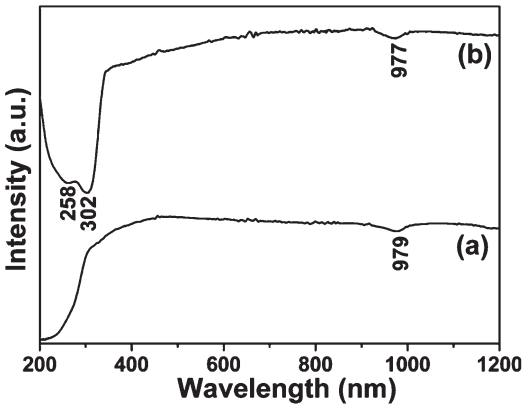

Fig. 5 Diffuse reflectance spectra of $NaYF_4$: 1 mol%Tb^{3+}, 5%Yb^{3+} (a) and L-$NaYF_4$: 1 mol%Tb^{3+}, 5%Yb^{3+} (b).

stretching vibration. The bands at 1592 and 1403 cm^{-1} can be assigned to the asymmetric (ν_{as}) and symmetric (ν_s) stretching vibration of the carboxyl group in the citric acid molecule, respectively.[36] In the FTIR spectra of the L-$NaYF_4$: 1 mol%Tb^{3+}, 5 mol%Yb^{3+}, the absorption bands around 3227 cm^{-1} and 3041 cm^{-1} are caused by the ν_{O-H} (hydrogen bond inside molecule) vibration peak and the C–H stretching vibration of H_4L, respectively.[37] Moreover, the spectra show two peaks at 1543 cm^{-1} and 1439 cm^{-1}, corresponding to the asymmetric (ν_{ascoo-}) and symmetric stretching vibration (ν_{scoo-}) of carboxyl, respectively.[37] The absorption peaks at 570–910 cm^{-1} are assigned to the out-of-plane bending vibrations of benzene rings. At the same time, the $\nu_{C=O}$ stretching vibration at 1660–1770 cm^{-1} still exist, implying that the carboxyls for H_4L have partial coordination with RE^{3+} by acid radicals.

The representative UV-vis absorption spectra of H_4L, L-$NaYF_4$: 1 mol%Tb^{3+}, 5 mol%Yb^{3+} are drawn in Fig. 4. For H_4L, three absorption bands located around 214, 249 and 294 nm are observed, corresponding to the π–π* transition absorption of the H_4L. Similarly, the absorption bands at about 216, 255 and 295 nm were observed for the L-$NaYF_4$: 1 mol%Tb^{3+}, 5 mol%Yb^{3+} nanoparticles, respectively. The slight red-shifts of three bands in L-$NaYF_4$: 1 mol%Tb^{3+}, 5 mol%Yb^{3+} nanoparticles can be attributed to the increasing conjugation after the H_4L are bonded to the surface of the nanoparticles in contrast to the H_4L.[33] The UV-vis absorption spectra of $NaYF_4$: 1 mol%Tb^{3+}, x mol%Yb^{3+} (x = 1, 3, 5, 10) samples also are measured, and no absorption transition is observed. These results demonstrate that H_4L is actually bonded to the surface of the nanoparticles.

The diffuse reflection spectra of different samples are recorded at room temperature. The representative diffuse reflection spectra of $NaYF_4$: 1 mol%Tb^{3+}, 5 mol%Yb^{3+} and L-$NaYF_4$: 1 mol%Tb^{3+}, 5 mol%Yb^{3+} are drawn in Fig. 5. For the diffuse reflectance spectra of $NaYF_4$: 1 mol%Tb^{3+}, 5 mol%Yb^{3+}, the absorption edge is clearly observed in UV region, which is attributed to the parity allowed transition $4f^8 \rightarrow 4f^7$5d of Tb^{3+} ions. The absorption bands between 900 and 1050 nm are corresponding to the $^2F_{5/2}$–$^2F_{7/2}$ transition of Yb^{3+} ions. In the diffuse reflectance spectra of L-$NaYF_4$: 1 mol%Tb^{3+}, 5 mol%Yb^{3+}, there are three absorption bands between 200 and 400 nm, which are attributed to the π–π* transition absorption of the H_4L in the UV region, and absorption bands between 900 and 1050 nm corresponding to the $^2F_{5/2}$–$^2F_{7/2}$ transition of Yb^{3+} in near-infrared region. The parity forbidden f–f transition of Tb^{3+} ions cannot be observed because of lower component of Tb^{3+} ions (1 mol%) in UV-vis region for the diffuse reflection spectra of all samples.

Photoluminescence properties

At room temperature the NIR photoluminescence spectra of the different samples are detected, and the representative ones for $NaYF_4$: 1 mol%Tb^{3+}, 5 mol%Yb^{3+} and L-$NaYF_4$: 1 mol%Tb^{3+}, 5 mol%Yb^{3+} nanoparticles are shown in Fig. 6(a). In the excitation spectra of $NaYF_4$: 1 mol%Tb^{3+}, 5 mol%Yb^{3+} sample by monitoring $^2F_{5/2} \rightarrow {}^2F_{7/2}$ transition of Yb^{3+} at 979 nm, a band centered at 270 nm assigned to the characteristic $4f^8$–$4f^7$5d transition of Tb^{3+} is observed.[38] Upon the excitation of 270 nm, an emission peak located at 979 nm and several weak shoulders owing to transitions among different Stark levels of ^2F_J (J = 5/2, 7/2) of Yb^{3+} ions are observed. This resulted from the cooperative energy transition between Tb^{3+} ions with Yb^{3+} ions through downconversion quantum cutting.[12,13] It is worthy to note that a strong and broad band from 230 nm to 530 nm is observed by monitoring $^2F_{5/2} \rightarrow {}^2F_{7/2}$ transition of Yb^{3+} at 977 nm in the excitation spectra of L-$NaYF_4$: 1 mol%Tb^{3+}, 5 mol%Yb^{3+} sample, which are attributed to the π–π* transition absorption of the H_4L. Upon the excitation of π–π* transition of the H_4L, an intense emission peak located at 977 nm and several weak shoulders owing to transitions among different Stark levels of ^2F_J (J = 5/2, 7/2) of Yb^{3+} ions are observed.

To investigate the pathway of energy transfer in hybrid nanoparticles, the photoluminescence spectra of the different samples in UV-vis region were detected at room temperature. The representative excitation and emission spectra of $NaYF_4$: 1 mol%Tb^{3+}, 5 mol%Yb^{3+} and L-$NaYF_4$: 1 mol%Tb^{3+}, 5 mol%Yb^{3+} are shown in Fig. 6(b). The excitation

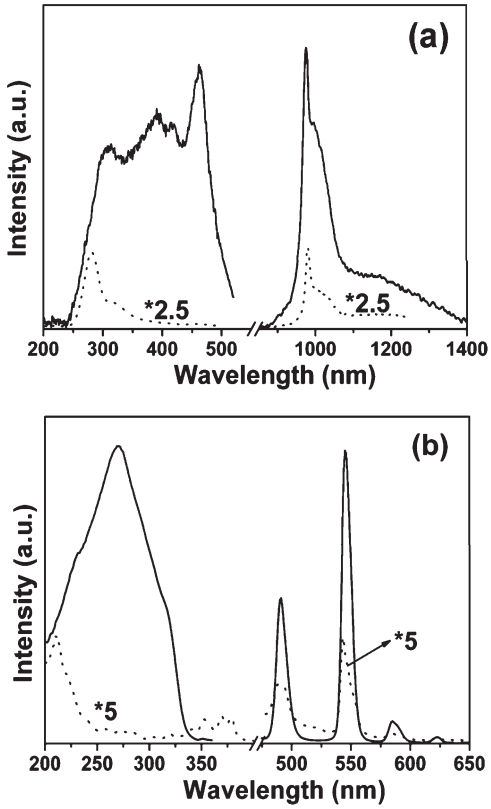

Fig. 6 NIR excitation and emission spectra of $NaYF_4$: 1 mol%Tb^{3+}, 5%Yb^{3+} (dot line) and L-$NaYF_4$: 1 mol%Tb^{3+}, 5%Yb^{3+} (solid line). (a) UV-Vis excitation and emission spectra of $NaYF_4$: 1 mol%Tb^{3+}, 5%Yb^{3+} (dot line) and (b) L-$NaYF_4$: 1 mol%Tb^{3+}, 5%Yb^{3+} (solid line).

spectra were obtained by monitoring the emission of the $^5D_4$–$^7F_5$ transition of Tb^{3+} ions at 545 nm (left of Fig. 6(b)).

For the $NaYF_4$: 1 mol%Tb^{3+}, 5 mol%Yb^{3+} nanoparticles, the excitation spectra are composed of the characteristic $4f^8$–$4f^75d$ transitions of the Tb^{3+} configuration and forbidden f–f transitions of within the Tb^{3+} $4f^8$ configuration. The two bands at 213 and 255 nm are associated with the lowest low-spin and high-spin $4f^{n-1}$–5d transitions of Tb^{3+} ions.[39] The excitation bands in the longer wavelength region (280–400 nm) can be assigned as the transitions from the $^7F_6$ ground state to the different excited states of Tb^{3+} within the Tb^{3+} $4f^8$ configuration, that is, 284 nm ($^5I_6$), 303 nm ($^5H_6$), 319 nm ($^5D_0$), 340 nm ($^5G_2$), 352 nm ($^5D_2$), 369 nm ($^5G_6$), and 378 nm ($^5D_3$), respectively.[40] For the excitation spectra of L-$NaYF_4$: 1 mol%Tb^{3+}, 5 mol%Yb^{3+} nanoparticles, it can be seen clearly that the excitation spectra present an intense, broad band from 200 to 355 nm (see the left solid line of Fig. 6(b)), which proves that the Tb^{3+} in $NaYF_4$ nanoparticles is excited *via* the antenna of H_4L. Upon excitation at 272 nm for the L-$NaYF_4$: 1 mol%Tb^{3+}, 5 mol%Yb^{3+} nanoparticles, the characteristic green emission bands of Tb^{3+} ions are observed (see the right solid line of Fig. 6(b)), corresponding to the $^5D_4 \rightarrow {}^7F_J$ (J = 4–6) transitions. The strongest emission is centered at around 545 nm due to the $^5D_4 \rightarrow {}^7F_5$ transition. These results demonstrate that the excitation energy is first transferred from H_4L to Tb^{3+} ions. So, the energy transition pathway in the hybrid systems consists of an initial strong absorption of ultraviolet energy that excites H_4L to the excited singlet (S_1) state, followed by an energy migration *via* intersystem crossing from the S1 state to triplet (T) state of H_4L. The energy is then nonradiatively transferred from the lowest triplet state of H_4L to a resonance state ($^5D_4$) of coordinated Tb^{3+} ions. By cooperative energy transition through downconversion quantum cutting, the Tb^{3+} ions then transfer the energy to the Yb^{3+} ions, which in turn undergo a multiphoton relaxation and subsequent emission in the near infrared region. The schematic diagram of molecular structure of H_4L and the energy transfer in hybrid nanoparticles is shown in Fig. 7.

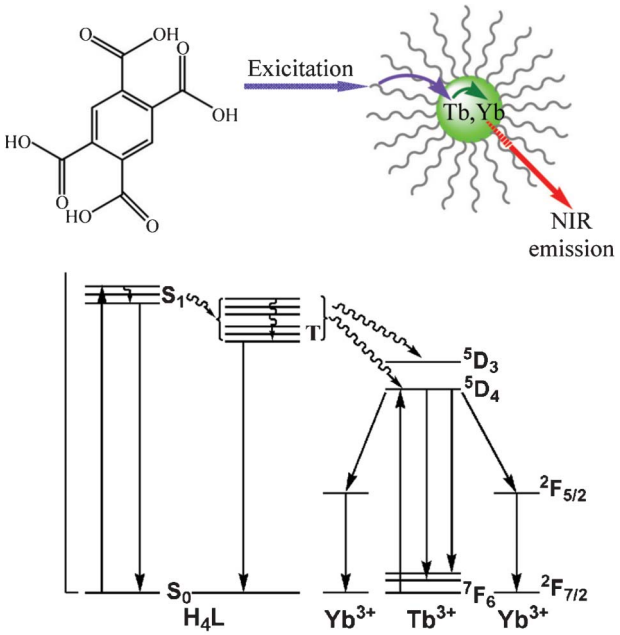

Fig. 7 The schematic diagram of molecular structure of H_4L and the energy transfer in hybrid nanoparticles.

The fluorescence decay curves for the $^5D_4 \rightarrow {}^7F_5$ transition of Tb^{3+} ions at 545 nm in different samples were measured at room temperature. Fig. 8 shows the representative fluorescence decay curves for the $^5D_4$–$^7F_5$ transitions of Tb^{3+} ions in the $NaYF_4$: 1 mol%Tb^{3+}, 5 mol%Yb^{3+} and L-$NaYF_4$: 1 mol%Tb^{3+}, 5 mol%Yb^{3+} samples, respectively. It can be seen that the fluorescence decays non-exponentially, which imply that the energy transfer between Tb^{3+} ions and Yb^{3+} ions occurs. All of the decay curves can be well fitted by a function as $I = I_1 \exp(-\tau_1/t) + I_2 \exp(-\tau_2/t)$, where τ_1 and τ_2 are the decay time constants, respectively. I_1 and I_2 present the ratios of the decay time components, respectively. The detailed luminescence lifetimes of Tb^{3+} ions in different samples are listed in Table 1. The results show that the lifetime of different samples decreases rapidly with increasing the concentration of Yb^{3+}, implying the occurrence of energy transfer from Tb^{3+} ions to Yb^{3+} ions. The lifetime of the L-$NaYF_4$: 1 mol%Tb^{3+}, x mol%Yb^{3+} (x = 1, 3, 5, 10) become longer than that of the $NaYF_4$: 1 mol%Tb^{3+}, x mol%Yb^{3+} (x = 1, 3, 5, 10), which can be attributed to the influence of the surrounding media (H_4L).

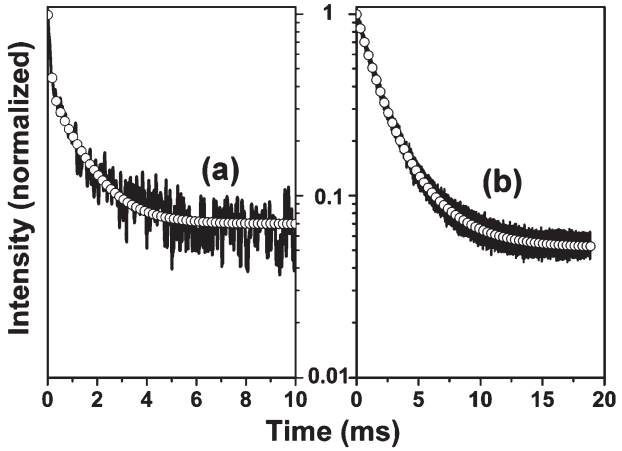

Fig. 8 Luminescence decay curves of the $^5D_4$–$^7F_5$ transition of Tb^{3+} in $NaYF_4$: 1 mol%Tb^{3+}, 5%Yb^{3+} (a) and L-$NaYF_4$: 1 mol%Tb^{3+}, 5%Yb^{3+} (b). The solid lines are experimental data, and the white circles are fitting functions.

The radiative lifetime can be written as

$$\tau_R \approx \frac{1}{f(ED)} \frac{{\lambda_0}^2}{[\frac{1}{3}(n^2+2)]^2 n} \quad (1)$$

where $f(ED)$ is the oscillator strength for the electronic dipole transition, λ_0 is the wavelength in vacuum and n is the refractive index of the material. R. S. Meltzer *et al.*[41] observe that the radiative fluorescence lifetime of Y_2O_3:Eu^{3+} nanocrystals is dependent not only on the refractive index, but also on the surrounding medium. They deduced that in nanoparticles, n in eqn (1) should be substituted by the effective refractive index $n_{\text{eff}}(x) = x\,n + (1 - (x)\,n_{\text{med}}$, where x is the filling factor showing what fraction of the space is occupied by the nanoparticles, and n_{med} is the refractive index of the surrounding media. In the present case, the Tb^{3+} ions are surrounded by $NaYF_4$ crystal in the L-$NaYF_4$:Tb^{3+}, Yb^{3+}. The refractive index values are 1.55 for $NaYF_4$ [42] in L-$NaYF_4$:Tb^{3+}, Yb^{3+} and 1.71 for H_4L in lanthanide complexes of H_4L. The decreased refractive index of the Tb^{3+} ions surrounding media will lead n_{eff} to be smaller than the refractive index of the complex n which would induce the increase of radiative lifetime. It is important to note that the τ_1 for the L-$NaYF_4$:Tb^{3+}, Yb^{3+} samples are longer than that τ_1 for $NaYF_4$:Tb^{3+}, Yb^{3+} samples. The cause is that the Tb^{3+} in the nanomaterials locates in different environments. Owing to the large surface to volume ratio of nanomaterials, Tb^{3+} in the nanoparticles locates two different environments in general, *i.e.* at the core of the particles and at or near the surface of particles, respectively. The τ_1 can be attributed to the luminescence decay from Tb^{3+} located at or near the surface of the nanomaterials. The shield from the quenching effect of water and ''antenna effect'' of H_4L over the surface of nanoparticles make the lifetime of Tb^{3+} located at or near the surface of the nanomaterials become longer.

Conclusions

In conclusion, we have synthesized ultra-small-sized $NaYF_4$:Tb^{3+}, Yb^{3+} nanoparticles and hybrid L-$NaYF_4$:Tb^{3+}, Yb^{3+} nanoparticles. Their DC QC PL properties have been studied contrastively at room temperature. Combining the antenna and shield effect provided by organic H_4L with the protection of inorganic matrices $NaYF_4$, the hybrid nanoparticles display a broad absorption in the UV-vis domain, strong NIR emission at about 1000 nm that matches to the energy of Si band gap of Si-based solar cells, and longer lifetimes as a result of energy transfer from the organic H_4L to Tb^{3+} ions and then to Yb^{3+} ions. The results will provide a new path for developing organic–inorganic hybrid luminescent materials as spectral converters to improve the efficiency of Si solar cells.

Acknowledgements

This project was financially supported by National Basic Research Program of China (2010CB327704), and the National Natural Science Foundation of China (NSFC 51172227, 21221061).

Notes and references

1 R. T. Wegh, H. Donker, K. D. Oskam and A. Meijerink, *Science*, 1999, **283**, 663.
2 P. Vergeer, T. J. H. Vlugt, M. H. F. Kox, M. I. den Hertog, J. P. J. M. van der Eerden and A. Meijerink, *Phys. Rev. B: Condens. Matter Mater. Phys.*, 2005, **71**, 014119.
3 T. J. Lee, L. Y. Luo, T. M. Chen, E. W. G. Diau, B. M. Cheng and C. Y. Tung, *Appl. Phys. Lett.*, 2006, **89**, 131121.
4 H. Y. Tzenga, B. M. Cheng and T. M. Chen, *J. Lumin.*, 2007, **122–123**, 917.
5 J. M. Meijer, L. Aarts, B. M. van der Ende, T. J. H. Vlugt and A. Meijerink, *Phys. Rev. B: Condens. Matter Mater. Phys.*, 2010, **81**, 035107.
6 L. Aarts, B. M. van der Ende and A. Meijerink, *J. Appl. Phys.*, 2009, **106**, 023522.
7 Q. Y. Zhang, C. H. Yang and Y. X. Pan, *Appl. Phys. Lett.*, 2007, **90**, 021107.
8 Q. Y. Zhang and X. F. Liang, *J. Soc. Inf. Disp.*, 2008, **16**, 755.
9 B. S. Richards and A. Shalav, *Synth. Met.*, 2005, **154**, 61.
10 B. S. Richards, *Sol. Energy Mater. Sol. Cells*, 2006, **90**, 2329.
11 B. S. Richards, *Sol. Energy Mater. Sol. Cells*, 2006, **90**, 1189.
12 S. Ye, B. Zhu, J. Chen, J. Luo and J. R. Qiu, *Appl. Phys. Lett.*, 2008, **92**, 141112.
13 Y. Wang, L. Xie and H. Zhang, *J. Appl. Phys.*, 2009, **105**, 023528.
14 J. Ueda and S. Tanabe, *J. Appl. Phys.*, 2009, **106**, 043101.
15 G. Lakshminarayana and J. R. Qiu, *J. Alloys Compd.*, 2009, **481**, 582.
16 X. Y. Huang and Q. Y. Zhang, *J. Appl. Phys.*, 2009, **105**, 053521.
17 Y. Tu, J. J. Zhou, X. F. Liu, S. Ye and J. R. Qiu, *Opt. Express*, 2010, **18**, 9671.
18 Q. Zhang, G. R. Chen, G. Zhang, J. R. Qiu and D. P. Chen, *J. Appl. Phys.*, 2010, **107**, 023102.

19 J. D. Chen, H. Guo, Z. Q. Li, H. Zhang and Y. X. Zhuang, *Opt. Mater.*, 2010, **32**, 998.
20 B. M. van der Ende, L. Aarts and A. Meijerink, *Adv. Mater.*, 2009, **21**, 3073.
21 B. M. van der Ende, L. Aarts and A. Meijerink, *Phys. Chem. Chem. Phys.*, 2009, **11**, 11081.
22 J. J. Eilers, D. Biner, J. T. van Wijngaarden, K. Krämer, H. U. Güdel and A. Meijerink, *Appl. Phys. Lett.*, 2010, **96**, 151106.
23 D. Q. Chen, Z. Hao, F. Li and G. Hai, *Mater. Chem. Phys.*, 2011, **128**, 191.
24 D. Serrano, A. Braud, J.-L. Doualan, P. Camy, A. Benayad, V. Ménard and R. Moncorgé, *Opt. Mater.*, 2011, **33**, 1028.
25 H. Lin, D. Q. Chen, Y. L. Yu, A. P. Yang and Y. S. Wang, *Opt. Lett.*, 2011, **36**, 876.
26 D. Q. Chen, Y. S. Wang, Y. L. Yu, P. Huang and F. Y. Weng, *J. Appl. Phys.*, 2008, **104**, 116105.
27 D. Q. Chen, Y. S. Wang, Y. L. Yu, P. Huang and F. Y. Weng, *Opt. Lett.*, 2008, **33**, 1884.
28 D. Q. Chen, Y. L. Yu, H. Lin, P. Huang, Z. F. Shan and Y. S. Wang, *Opt. Lett.*, 2010, **35**, 220.
29 W. L. Zhou, J. Yang, J. Wang, Y. Li, X. J. Kuang, J. K. Tang and H. B. Liang, *Opt. Express*, 2012, **20**, A510.
30 M. H. Qu, R. Z. Wang, Y. Chen, Y. Zhang, K. Y. Li and H. Yan, *J. Lumin.*, 2012, **132**, 1285.
31 A. Guille, A. Pereira, G. Breton, A. Bensalah-Ledoux and B. Moine, *J. Appl. Phys.*, 2012, **111**, 043104.
32 V. Sudarsan, F. C. J. M. van Veggel, R. A. Herring and M. Raudsepp, *J. Mater. Chem.*, 2005, **15**, 1332.
33 Z. W. Quan, D. M. Yang, P. P. Yang, X. M. Zhang, H. Z. Lian, X. M. Liu and J. Lin, *Inorg. Chem.*, 2008, **47**, 9509.
34 A. M. Cross, P. S. May, F. C. J. M. van Veggel and M. T. Berry, *J. Phys. Chem. C*, 2010, **114**, 14740.
35 R. D. Shannon, *Acta. Cryst.*, 1976, **A32**, 751.
36 L. Y. Wang and Y. D. Li, *Nano Lett.*, 2006, **6**, 1645.
37 S. W. Li, X. Zhang, Z. Y. Hou, Z. Y. Cheng, P. A. Ma and J. Lin, *Nanoscale*, 2012, **4**, 5619.
38 (*a*) L. G. Deshazeer and G. H. Dieke, *J. Chem. Phys.*, 1963, **38**, 2190; (*b*) C. X. Li, Z. W. Quan, J. Yang, P. P. Yang and J. Lin, *Inorg. Chem.*, 2007, **46**, 6329.
39 S. Piotr, L. Radosław, G. Marek, D. D. Grażyna and R. R. Witold, *Opt. Mater.*, 2007, **30**, 146.
40 K. S. Thomas, S. Singh and G. H. Dieke, *J. Chem. Phys.*, 1963, **38**, 2180.
41 R. S. Meltzer, S. P. Feofilov, B. Tissue and H. B. Yuan, *Phys. Rev. B: Condens. Matter*, 1999, **60**, 14012.
42 Z. W. Yang, K. Zhu, Z. G. Song, X. Yu, D. C. Zhou, Z. Y. Yin, L. Yan and J. B. Qiu, *Appl. Phys. A: Mater. Sci. Process.*, 2011, **103**, 995.